Radiation Perpendicular to the Symmetry Axis of Prolate and Oblate Cavities

Sean P. Fitzgerald and William Strieder
Dept. of Chemical Engineering, University of Notre Dame, Notre Dame, IN 46556

Thermal radiation heat transport within prolate and oblate ellipsoidal cavities was examined. The axisymmetric anisotropy of the cavity shape gives rise to a thermal radiation conductivity tensor with principal axes components parallel ($\lambda_{r,\parallel}$) *and perpendicular* ($\lambda_{r,\perp}$) *to the symmetry axis. The prolate* ($\lambda_{r,\perp}$) *and oblate* ($\tilde{\lambda}_{r,\perp}$) *transverse components are calculated and compared with well-known results from the kinetic theory of transport across cylindrical and within slit void geometries. The use of* $\lambda_{r,\perp}$ *and* $\tilde{\lambda}_{r,\perp}$, *along with earlier results for* $\lambda_{r,\parallel}$ *and* $\tilde{\lambda}_{r,\parallel}$, *in well-known effective conductivity equations for spheroidal inclusions within a solid matrix, provides a means to rigorously treat cavity orientation and shape in high-temperature heat transport across porous materials. To facilitate the calculations and produce readily usable equations, a variational principle is used.*

Introduction

Examples of engineering applications where void radiation transport plays a significant role include void transport in porous high-temperature fire brick (Ganguley and Hasselman, 1976), cavity heat transfer across ceramic nuclear fuel elements (Marino 1969, 1971; Takahashi and Kikuchi, 1980), the passage of exothermic reaction heat through porous reactants and products during the combustion synthesis of ceramics (Varma et al., 1990), and pore-space heat transfer in low-pressure cryogenic insulation (Kaganer, 1969). The engineering property needed for thermal calculations is λ_e, the heterogeneous material's effective thermal conductivity. In practice, λ_e is usually estimated from the solid conductivity λ_s and a suitably averaged, model void radiation conductivity λ_r. Other void transport mechanisms can also be included in λ_e (Argo and Smith, 1953; Smith, 1970) and are normally represented by diffusive-type coefficients, such as the heat-transfer convection coefficient. Note that the λ_r form will depend on the void shape and can become a tensor for an anisotropic cavity.

Expressions for λ_r are always useful for heat-transfer calculations. In a review paper, Vortmeyer (1980) presented a table of empirical and derived radiation conductivities for heterogeneous systems, including both cavity and dispersed solid cases. Vortmeyer's cavity-λ_r-type equations were based only on the spherical pore and flux across parallel-plates pore models. In nuclear fuel elements, where cavity aspect ratios can be significant, Marino (1971) attempted to treat cavity anisotropy by using prolate and oblate spherical cavity models. For lack of an existing void radiation conductivity for these cavity geometries, he proposed

$$\lambda_r\,(\text{marino}) \approx 3\epsilon\sigma\bar{T}^3 d_p \tag{1}$$

where ϵ is the cavity surface emissivity, $\bar{T}$ is the average cavity surface temperature, σ is the Stephan-Boltzmann constant, and d_p is the longest dimension of the pore in the direction of heat flow. As we shall soon see, Eq. 1 does not always work well, and a need exists for straightforward methods to derive λ_r formulas.

In cases where the pore microstructural lengths are small compared to the overall dimensions of the porous material, and the local temperature drop ΔT over micropore dimensions is small compared to the average local temperature $\bar{T}$, ($\Delta T \ll \bar{T}$), a porous material effective conductivity λ_e can be shown to exist (Whitaker, 1980). A rigorous variational upper bound principle can then be constructed for λ_e. We consider an optically opaque solid surrounding a cavity void volume in which heat transfer occurs by surface radiative processes. The cavity-solid interface is a gray body with emissivity ϵ, and also a cosine-law emitter and reflector (Siegel and Howell, 1992). The transport equations are based on a Fourier solid surrounding the void, but the radiation inside the void is gov-

---

Correspondence concerning this article should be addressed to W. Strieder.

erned by an interfacial flux boundary condition and an exact nonlocal surface-to-surface integral equation with a differential view factor (Fitzgerald and Strieder, 1997a).

The corresponding two-Fourier problem, that is, a solid of conductivity λ_s and an anisotropic prolate or oblate inclusion with Fourier conductivities $\lambda_{r,\parallel}$ parallel to and $\lambda_{r,\perp}$ perpendicular to the axis of symmetry, can be exactly (Carslaw and Jaeger, 1959). If this temperature in the surrounding solid in terms of its fundamental unknown constants is selected as the trial temperature T^*, the trial radiosity B^* can be generated by inserting the trial temperature into the interfacial flux condition (Chiew and Glandt, 1983). Once these trial T^* and B^* are substituted into the λ_e variational principle (Fitzgerald and Strieder, 1997a), cavity radiation conductivity forms can be identified by comparing the optimized λ_e variational expression to the exact form of the two-phase Fourier effective conductivity, as they are identical for either the prolate or oblate cavities. An alternative procedure, along either principal axis direction ($\parallel$ or $\perp$), is to use the point in a plot of λ_e for an evacuated porous medium versus the solid conductivity λ_s, that the effective conductivity crosses the 45° line, and $\lambda_e = \lambda_s = \lambda_r$. Both methods give the same variational upper bound-estimate of λ_r.

When an ellipse $(x^2a^{-2} + y^2b^{-2} = 1)$ of semimajor axis a and semiminor axis b is rotated about the x-axis, a prolate cavity with x-axis symmetry is generated. It is customary to designate the shape with an eccentricity factor $\alpha = (1 - b^2a^{-2})^{1/2}$. In a recent article Fitzgerald and Strieder (1997a) derived the cavity radiation conductivity $\lambda_{r,\parallel}$ down along the symmetry axis. Of particular interest is the radiation conductivity down the long needle obtained in the limit $\alpha \to 1$,

$$\lambda_{r,\parallel}(\text{needle}) = 3\pi\sigma\bar{T}^3 b, \qquad 0 < \epsilon \le 1, \tag{2}$$

where σ is the Stephan-Boltzmann constant. To complete the cavity radiation conductivity calculation, the conductivity $\lambda_{r,\perp}$ in the direction of the other principal axis across the symmetry axis is calculated herein. The long needle $(\alpha \to 1)$ result corresponding to Eq. 2,

$$\lambda_{r,\perp}(\text{needle}) = (9/2)\pi\epsilon(4-\epsilon)^{-1}\sigma\bar{T}^3 b, \quad 0 \le \epsilon \le 1 \tag{3}$$

is given in terms of b, the radius of the largest circular cross-section of the prolate cavity. The length dimension b is used in the radiation conductivities (Eqs. 2 and 3) because b is the order of the average photon free path for surface-to-surface jumps in the needle cavity. When the same ellipse $(x^2a^{-2} + y^2b^{-2} = 1)$ is rotated about the y-axis, an oblate cavity is constructed with a characteristic eccentricity $\beta = (1 - b^2a^{-2})^{1/2}$. Note that, although b is the radius of the largest circular cross-section of the prolate cavity, its role as the dimension of the symmetry axis of the oblate cavity is quite different. Using the variational method outlined above Fitzgerald and Strieder (1997b) developed a general form for the radiation conductivity $\tilde{\lambda}_{r,\parallel}$ across the oblate cavity in the direction of the symmetry axis. For the special case of the thermal flux across a thin discus in the limit $\beta \to 1$, their cavity radiation conductivity takes the simple form

$$\tilde{\lambda}_{r,\parallel}(\text{discus}) = 6\epsilon(2-\epsilon)^{-1}\sigma\bar{T}^3 b, \quad 0 \le \epsilon \le 1. \tag{4}$$

To complement this result, the void radiation conductivity $\tilde{\lambda}_{r,\perp}$ in the direction perpendicular to the symmetry axis has also been derived in this paper. In the discus limit $(\beta \to 1)$, we will show that the $\tilde{\lambda}_{r,\perp}$ coefficient becomes singular according to the expression,

$$\tilde{\lambda}_{r,\perp}(\text{discus}) = [-3\ln(1-\beta)]\sigma\bar{T}^3 b, \quad 0 < \epsilon \le 1. \tag{5}$$

Again the results are written in terms of the fundamental photon free path dimension b, but in the oblate cavity b relates to a maximum slit width or parallel plate spacing.

Eq. 5 represents, to the best of our knowledge, the first time the exact closed algebraic form of the conductivity divergence for a long slit type geometry has appeared in the literature. In the previous related literature of the kinetic theory of Knudsen diffusion, Berman (1965) obtained the logarithmic singularity in a long slit, but only as an upper bound. While Marino's Eq. 1 does not agree closely with any of the more accurate λ_r results from Eqs. 2–5, the choice of a rather than the free path dimension b down the long needle symmetry axis is unfortunate as it leads to an incorrect infinity in Eq. 1 for $\lambda_{r,\parallel}$. On the other hand, for $\tilde{\lambda}_{r,\perp}$ perpendicular to the symmetry axis of the discus, the choice of the a rather than b is only half the problem, the other problem being that the correct $\ln(b/a)$ singularity of Eq. 5 is much milder than (a/b) predicted by Eq. 1.

In the next section, temperature and radiosity trial functions are presented for arbitrary direction of the applied thermal gradient. General λ_e expressions that include aspects of both anisotropy and orientation are obtained, and λ_r general forms are identified for the principal axes of prolate and oblate cavities. In the section on "Radiation Conductivities Perpendicular to the Symmetry Axis of Prolate and Oblate Cavities," explicit, readily usable equations for the radiation conductivity transverse to the symmetry axes of prolate and oblate cavities are given. Detailed derivation forms are presented in an Appendix. This section is followed by a discussion of prolate $\lambda_{r,\perp}$ and oblate $\tilde{\lambda}_{r,\perp}$ results and the various limits. In the final section, several equations are presented for λ_e in terms of the anisotropic, spheroidal void radiation conductivities.

Effective Thermal Conductivities For Prolate and Oblate Cavities of Arbitrary Orientation

This section examines the problem of general orientation of the prolate and oblate voids, or equivalently a thermal gradient $\boldsymbol{\theta}$ applied in an arbitrary direction far from the cavity. The purpose of this section is to give generalized trial functions for prolate and oblate cavities of arbitrary orientation, to demonstrate the tensor nature of the effective conductivity for these anisotropic cavities, to point out that principal axis forms evolve naturally from the variational approach, and to present new equations for temperature gradients applied perpendicular to the symmetry axis. Once the effective conductivity tensor is diagonalized, each principal axis term must be optimized independently, and each generates a different void radiation conductivity. For brevity, only an outline of the derivations is given here. The optimization of each effective conductivity diagonal element to obtain the principal axis forms of the effective conductivity and void radiation coefficient is similar to those done in Fitzgerald and Strieder

(1997a,b) and the reader is referred to these sources for details. This is also true for both the development of the radiosity trial from the temperature trial function and for their insertion into the variational principle. Furthermore, the results found in this section will be used in the effective conductivity and void radiation conductivity usage discussion in the "Conclusion" section.

The prolate and oblate shapes were both generated from the same ellipse ($x^2a^{-2}+y^2b^{-2}=1$) by rotation, respectively, around $2a$ or $2b$ as the symmetry axis. Although the equations in this section are stated in the prolate form, the corresponding functions for the oblate cavity can be obtained simply by interchanging a and b. A tilde over a symbol denotes the oblate geometry.

The corresponding two-phase Fourier problem of an anisotropic prolate (or oblate) inclusion with different Fourier conductivities $\lambda_{r,\parallel}$ parallel and $\lambda_{r,\perp}$ perpendicular to the symmetry axis can be solved exactly (Carslaw and Jaeger, 1959). Their temperature solution exterior to the spheroidal inclusion serves as the trial temperature for the cavity radiation case

$$T^* = \bar{T} + \boldsymbol{\theta}\cdot\boldsymbol{r} + P_{\parallel}[G_{\parallel}(\xi)/G_{\parallel}(0)]\boldsymbol{\theta}_{\parallel}\cdot\boldsymbol{r} + P_{\perp}[G_{\perp}(\xi)/G_{\perp}(0)]\boldsymbol{\theta}_{\perp}\cdot\boldsymbol{r} \tag{6a}$$

$$G_{\parallel}(\xi) = \frac{1}{2}ab^2\int_{\xi}^{\infty} du(a^2+u)^{-3/2}(b^2+u)^{-1} \tag{6b}$$

and

$$G_{\perp}(\xi) = \frac{1}{2}ab^2\int_{\xi}^{\infty} du(a^2+u)^{-1/2}(b^2+u)^{-2} \tag{6c}$$

The ellipsoidal coordinate ξ has a value of zero on the surface of the cavity, $\boldsymbol{r}$ is a vector from from the center of the prolate (oblate) cavity, $\bar{T}$ is an average cavity surface temperature, and $\boldsymbol{\theta}_{\parallel}$ and $\boldsymbol{\theta}_{\perp}$ are vector components of $\boldsymbol{\theta}$ parallel and perpendicular to the symmetry axis. The functions $G_{\parallel}$ and $G_{\perp}$ are listed in integral form for convenience and have been evaluated by Marino (1971). The temperature naturally divides into contributions in the principal axis directions with variational parameters $P_{\parallel}$ and $P_{\perp}$. The trial radiosity B^* is also separated into components parallel and perpendicular to the symmetry axis

$$B^* = A + C\bar{T} + C\mu_{\parallel}[(1+P_{\parallel})\boldsymbol{\theta}_{\parallel}\cdot\boldsymbol{r} + \omega_{\parallel}\boldsymbol{\theta}_{\parallel}\cdot\boldsymbol{\eta}] + C\mu_{\perp}[(1+P_{\perp})\boldsymbol{\theta}_{\perp}\cdot\boldsymbol{r} + \omega_{\perp}\boldsymbol{\theta}_{\perp}\cdot\boldsymbol{\eta}] \tag{7a}$$

where

$$A = -3\sigma\bar{T}^4 \tag{7b}$$

and

$$C = 4\sigma\bar{T}^3 \tag{7c}$$

The trial radiosity is defined only on the void–solid interface Σ, and $\boldsymbol{\eta}$ is the surface normal at $\boldsymbol{r}$ on Σ pointing into the cavity. The sets of variational parameters $\{\mu_{\parallel}, \omega_{\parallel}, P_{\parallel}\}$ and $\{\mu_{\perp}, \omega_{\perp}, P_{\perp}\}$ are to be independently optimized to obtain the best effective conductivity. $\tilde{T}^*$ and $\tilde{B}^*$ are the oblate forms obtained when a and b are interchanged in Eqs. 6 and 7.

For an arbitrary orientation of $\boldsymbol{\theta}$, the effective conductivity becomes a dyadic $\boldsymbol{\lambda}_e$, and the vector average heat flux $\boldsymbol{Q}$ is given by

$$\boldsymbol{Q} = -\boldsymbol{\lambda}_e\cdot\boldsymbol{\theta} \tag{8}$$

Substitution of Eq. 8 and the trial functions T^*, B^* of Eqs. 6a–7c, respectively, into Eqs. 27 and the variation principle Eq. 18 of Fitzgerald and Strieder (1997a) yields a variational form for the effective conductivity, quadratic in the vector components $\boldsymbol{\theta}_{\parallel}$ and $\boldsymbol{\theta}_{\perp}$

$$\boldsymbol{\theta}\cdot\boldsymbol{\lambda}_e\cdot\boldsymbol{\theta} \leq \Lambda_{\parallel}\{\mu_{\parallel}, \omega_{\parallel}, P_{\parallel}\}\theta_{\parallel}^2 + \Lambda_{\perp}\{\mu_{\perp}, \omega_{\perp}, P_{\perp}\}\theta_{\perp}^2 \tag{9}$$

The cross terms involving $\boldsymbol{\theta}_{\parallel}$ and $\boldsymbol{\theta}_{\perp}$ vanish in Eq. 9 due to the axisymmetric nature of the prolate and oblate cavities. The same type of diagonalized quadratic form of the effective conductivity-$\boldsymbol{\theta}$ scalar product is found for the corresponding two-phase Fourier problem, but the mathematical details of the derivation are different owing to the different physical mechanisms of transport in the inclusion. For an arbitrary selection of the coordinate axes, the tensor components of $\boldsymbol{\lambda}_e$ can be obtained from the variational expression Eq. 9 by inserting the components $\{\theta_x, \theta_y, \theta_z\}$ into both sides.

On the other hand, the selection of either of the directions $\boldsymbol{\theta}_{\parallel}$ or $\boldsymbol{\theta}_{\perp}$ for $\boldsymbol{\theta}$ in Eq. 9 generates two expressions

$$\lambda_{e,\parallel} \leq \Lambda_{\parallel}\{\mu_{\parallel}, \omega_{\parallel}, P_{\parallel}\} \tag{10a}$$

and

$$\lambda_{e,\perp} \leq \Lambda_{\perp}\{\mu_{\perp}, \omega_{\perp}, P_{\perp}\} \tag{10b}$$

where the Λ terms of either Eq. 10a or 10b can be optimized independently. For the prolate cavity, the $\Lambda_{\parallel}$ form of Eq. 10a and the associated $\lambda_{r,\parallel}$ have already been developed in Fitzgerald and Strieder (1997a) and the oblate cavities $\tilde{\Lambda}_{\parallel}$ and $\tilde{\lambda}_{r,\parallel}$ were presented in Fitzgerald and Strieder (1997b) for radiative conductivities parallel to their symmetry axes. The optimization of Eq. 10b with respect to $\omega_{\perp}$ and $P_{\perp}$ produces a variational form of $\lambda_{e,\perp}$

$$\frac{\lambda_{e,\perp}}{\lambda_s} \leq 1 - \phi + \phi\frac{[1+G_{\perp}(0)]\lambda_{r,\perp}(\mu_{\perp}) - G_{\perp}(0)\lambda_s}{[1-G_{\perp}(0)]\lambda_s + G_{\perp}(0)\lambda_{r,\perp}(\mu_{\perp})} \tag{11}$$

where ϕ is the void fraction. If $\lambda_{r,\perp}(\mu_{\perp})$ is identified with the prolate conductivity $\lambda_{r,\perp}$ perpendicular to the symmetry axis, then Eq. 11 is the exact $\lambda_{e,\perp}$ solution form of the two-phase Fourier problem with an anisotropic prolate inclusion. The choice of the minimum value of $\lambda_{r,\perp}(\mu_{\perp})$ for the inequality (Eq. 11) is equivalent to selecting the most accurate value of the effective conductivity component $\lambda_{e,\perp}$. Upon interchange of the lengths a and b, both the variational Eq. 11 and the above discussion hold for an oblate cavity, that is, Eq. 11 holds with tildes implying the interchange.

Radiation Conductivities Perpendicular to the Symmetry Axis of Prolate and Oblate Cavities

The optimization of $\lambda_{r,\perp}(\mu_\perp)$ with respect to $\mu_\perp$ for both prolate and oblate cavities yields the model cavity radiation conductivity $\lambda_{r,\perp}$,

$$\lambda_{r,\perp} \leq \lambda_{r,\perp}(\mu_\perp) \tag{12}$$

Both the prolate and oblate voids have an optimum radiation conductivity perpendicular to the symmetry axis of the same general form,

$$\frac{\lambda_{r,\perp}}{Cb} = \frac{\chi_{0,\perp}\lambda_{0,\perp}(\chi_{2,\perp}+\lambda_{2,\perp}) - \chi_{0,\perp}\lambda_{1,\perp}^2 - \chi_{1,\perp}^2\lambda_{0,\perp}}{(\chi_{0,\perp}+\lambda_{0,\perp})(\chi_{2,\perp}+\lambda_{2,\perp}) - (\chi_{1,\perp}+\lambda_{1,\perp})^2} \tag{13}$$

but for oblate results tildes are used over all λs and χs in Eq. 13.

As was pointed out during the discussion of Eqs. 1–5 in the Introduction, it is convenient to express prolate and oblate forms of the radiation conductivities using the photon free path dimension b. However, in each of the cavity geometries b is different—it is a maximum circular cross-sectional radius in a prolate void and a maximum slit width for the oblate cavity. In addition there is a need to have the results in real functions in terms of the prolate $\alpha[=(1-b^2a^{-2})^{1/2}]$ and oblate $\beta[=(1-b^2a^{-2})^{1/2}]$ eccentricities, where b has a different meaning in each volume. Together these two conditions require separate expressions for the prolate χs, λs and oblate $\tilde{\chi}$s, $\tilde{\lambda}$s. Their derivations are addressed in the Appendix, and their forms are given below.

$$\chi_{0,\perp} = \epsilon(1-\epsilon)^{-1}(3/16)\{(2+\alpha^{-2})(1-\alpha^2)^{1/2} + (4\alpha^2-1)\alpha^{-3}\arcsin\alpha\} \tag{14}$$

$$\tilde{\chi}_{0,\perp} = \epsilon(1-\epsilon)^{-1}(3/32)\big\{2(3\beta^2-1)\beta^{-2}(1-\beta^2)^{-1} + (3\beta^2+1)\beta^{-3}\ln[(1+\beta)/(1-\beta)]\big\} \tag{15}$$

$$\chi_{1,\perp} = \tilde{\chi}_{1,\perp} = -\epsilon(1-\epsilon)^{-1}, \tag{16}$$

$$\tilde{\chi}_{2,\perp} = \epsilon(1-\epsilon)^{-1}(3/4)\{\alpha^{-2}(1-\alpha^2)^{1/2} + (2\alpha^2-1)\alpha^{-3}\arcsin\alpha\} \tag{17}$$

$$\chi_{2,\perp} = \epsilon(1-\epsilon)^{-1}(3/8)(1-\beta^2)\beta^{-2}\{-2+(1+\beta^2)\beta^{-1}\ln[(1+\beta)/(1-\beta)]\} \tag{18}$$

$$\lambda_{0,\perp} = (1-\epsilon)\epsilon^{-1}\chi_{2,\perp} \tag{19}$$

and

$$\tilde{\lambda}_{0,\perp} = (1-\epsilon)\epsilon^{-1}(1-\beta^2)^{-1}\tilde{\chi}_{2,\perp} \tag{20}$$

The integrals $\lambda_{1,\perp}$, $\lambda_{2,\perp}$, $\tilde{\lambda}_{1,\perp}$, and $\tilde{\lambda}_{2,\perp}$ have been reduced to two dimensions, but cannot be done analytically. These integrals are listed as Eq. A4 in the Appendix, and have been evaluated numerically by a double integral Newton-Cotes quadrature procedure (Ralston and Rabinowitz, 1978). As the integrals only depend on α^2 (or β^2), their numerical values can be fitted to Padé polynomial forms (McQuarrie, 1976). For the prolate cavity, the Padé representation of $\lambda_{1,\perp}$ is within 0.1% absolute accuracy

$$\lambda_{1,\perp} = \frac{-1+0.5793\alpha^2}{1-0.7818\alpha^2+0.0973\alpha^4} \tag{21}$$

and the $\lambda_{2,\perp}$ fit for the prolate cavity coefficient is also at least within 0.1%

$$\lambda_{2,\perp} = \frac{1-1.03009\alpha^2+0.12093\alpha^4}{1-1.32651\alpha^2+0.38434\alpha^4} \tag{22}$$

For the oblate cavity, the integrals $\tilde{\lambda}_{1,\perp}$ and $\tilde{\lambda}_{2,\perp}$ vanish as $\beta^2 \to 1$, and the Padé forms go to the correct limit. However, accuracy in the neighborhood of $\beta^2 = 1$ is difficult to maintain as the significant figures of the Padé coefficients tend to cancel out. The Padé expression for $\tilde{\lambda}_{1,\perp}$

$$\tilde{\lambda}_{1,\perp} = \frac{-1+2.951065\beta^2-2.946518\beta^4+1.039371\beta^6-0.043918\beta^8}{1-2.744013\beta^2+2.496350\beta^4-0.752317\beta^6} \tag{23}$$

is accurate within 0.12% provided $\beta^2 \leq 0.99$, and

$$\tilde{\lambda}_{2,\perp} = \frac{1-2.892672\beta^2+2.786536\beta^4-0.893864\beta^6}{1-2.094234\beta^2+1.270294\beta^4-0.157077\beta^6-0.017838\beta^8} \tag{24}$$

is accurate within 0.1% for all $\beta^2 \leq 0.99$. Similar Padé formulas for $\lambda_{r,\parallel}$ and $\tilde{\lambda}_{r,\parallel}$ have been calculated by Fitzgerald (1998).

Results for $\lambda_{r,\perp}$ and $\tilde{\lambda}_{r,\perp}$

If a composite is made up of an anisotropic prolate (or oblate) solid inclusion with Fourier conductivities $\lambda_{r,\parallel}$ and $\lambda_{r,\perp}$ (or $\tilde{\lambda}_{r,\parallel}$ and $\tilde{\lambda}_{r,\perp}$) parallel and perpendicular to the symmetry axis, respectively, surrounded by an isotropic solid of Fourier conductivity λ_s, analytical solutions can be obtained (Carslaw and Jaeger, 1959). The prolate Eq. 11 for $\lambda_{e,\perp}$ (or the oblate version $\tilde{\lambda}_{e,\perp}$), the effective composite conductivity perpendicular to the symmetry axis, is exact. However, the cavity void radiation problem $\lambda_{r,\perp}(\mu_\perp)$ (or the oblate $\tilde{\lambda}_{r,\perp}(\tilde{\mu}_\perp)$) in Eq. 11 still depends on a variational parameter $\mu_\perp$ (or $\tilde{\mu}_\perp$), and its optimization selects $\lambda_{r,\perp}$ (or $\tilde{\lambda}_{r,\perp}$), which is the radiation conductivity Eq. 12 that gives the very best value of $\lambda_{e,\perp}$ (or $\tilde{\lambda}_{e,\perp}$). This optimum prolate $\lambda_{r,\perp}$ (or oblate $\tilde{\lambda}_{r,\perp}$) is expressed by Eq. 13 in terms of $\chi_{i,\perp}$ (or $\tilde{\chi}_{i,\perp}$) and $\lambda_{i,\perp}$ (or $\tilde{\lambda}_{i,\perp}$) coefficients with $i = 0, 1, 2$. The $\chi_{i,\perp}$s and $\tilde{\chi}_{i,\perp}$s are given by Eqs. 14–18 in the terms of an emissivity factor $\epsilon(1-\epsilon)^{-1}$ multiplied by an analytical function of either the appropriate prolate α or oblate β eccen-

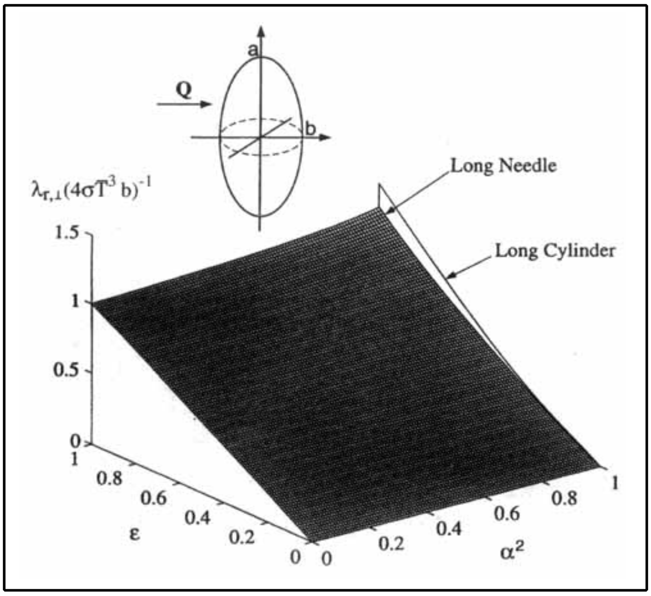

Figure 1a. Dimensionless radiation thermal conductivity $\lambda_{r,\perp}(4\sigma\bar{T}^3 b)^{-1}$, transverse to the symmetry axis of the prolate cavity, vs. the surface emissivity ϵ and squared eccentricity $\alpha^2(=1-b^2a^{-2})$.

A sketch of the prolate ellipsoid along with the overall heat flux vector Q is included. The single curve on the right-hand side is the corresponding $\lambda_{r,\perp}(4\sigma\bar{T}^3 b)^{-1}$ for a long cylinder of radius b.

tricity. The $\lambda_{0,\perp}$ and $\tilde{\lambda}_{0,\perp}$ of Eqs. 19–20 are also analytical functions, respectively, of α and β. The other coefficients can be obtained, $\lambda_{1,\perp}$, $\lambda_{2,\perp}$ in terms of α or $\tilde{\lambda}_{1,\perp}$, $\tilde{\lambda}_{2,\perp}$ in terms of β, numerically from Eqs. A4, A6a–A7b, and their oblate versions, all of which appear in the Appendix. These coefficients can also be estimated to within 0.1% from the Padé fits (Eqs. 21–24), but numerical computations of these coefficients are required to generate any values of $\tilde{\lambda}_{r,\perp}$ beyond $\beta^2 = 0.99$, as will appear in the oblate cavity void radiation conductivity discussion.

Prolate cavity, $\lambda_{r,\perp}$

Following the procedure above along with Eq. 7c for C, we have generated values of $\lambda_{r,\perp}(4\sigma\bar{T}^3 b)^{-1}$ for various degrees of elongation $\alpha^2(=1-b^2a^{-2})$ from zero to unity and emissivities ϵ also from zero to unity. The surface of Figure 1a demonstrates the overall behavior of this component of the cavity radiation conductivity, as well as its four possible limiting forms at $\alpha^2 \to 0$, $\alpha^2 \to 1$, $\epsilon \to 1$, and $\epsilon \to 0$. Figure 1a provides a prolate cavity sketch showing the direction of the overall heat transfer Q. As the subtle changes of $\lambda_{r,\perp}(4\sigma\bar{T}^3 b)^{-1}$ with α^2 for fixed $\epsilon < 0.8$ are difficult to see on the surface plot, Figure 1b includes these curves for the full range of emissivity values.

The trial temperature (Eq. 6) and radiosity functions (Eq. 7) are exact for the spherical cavity $\alpha^2 \to 0$, and the true $\lambda_{r,\perp}$ is known to be (Tsia and Strieder, 1985)

$$\lim_{\alpha^2 \to 0} \lambda_{r,\perp}(4\sigma\bar{T}^3 b)^{-1} = \epsilon \text{ (spherical void)} \qquad (25)$$

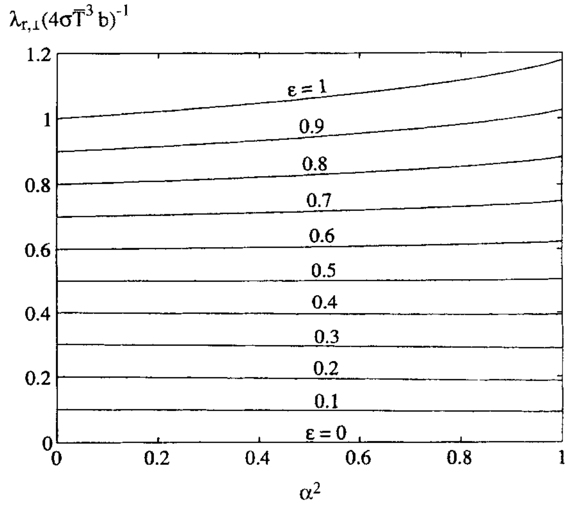

Figure 1b. Corresponding radiation conductivity vs. eccentricity for various emissivities.

The left-hand side of the dimensionless radiation conductivity surface in Figure 1a increases linearly from zero at $\epsilon = 0$ up to unity at $\epsilon = 1$. In the opposite limit $\alpha^2 \to 1$ of a long needle cavity on the right-hand side of the $\lambda_{r,\perp}(4\sigma\bar{T}^3 b)^{-1}$ surface of Figure 1a, Eq. 13 can be shown to vary with ϵ as

$$\lim_{\alpha^2 \to 1} \lambda_{r,\perp}(4\sigma\bar{T}^3 b)^{-1} = (9\pi/8)\epsilon(4-\epsilon)^{-1} \text{ (long needle)} \qquad (26)$$

where Eq. 3 has been recast in a dimensionless form appropriate for the discussion of Figures 1a and 1b. The radiation conductivity across the symmetry axis of a long right circular cylinder of radius b (Tsia and Strieder, 1986)

$$\lambda_{r,\perp}(4\sigma\bar{T}^3 b)^{-1} = 4\epsilon(4-\epsilon)^{-1} \text{ (long cylinder)} \qquad (27)$$

is also shown on the righthand side of Figure 1a for comparison. The conductivities (Eqs. 26 and 27) both have the same emissivity dependence, but the long needle result is a factor of $9\pi/32$ (≈ 0.88) smaller than the cylinder result. In the limit $a \gg b$, the needle conductivity (Eq. 26) can be obtained from the cylinder results (Eq. 27). The prolate spheroid may be represented by a stack of right circular cylinders with a common axis of symmetry and elliptically increasing, then decreasing local radii. Since any elemental cylinder can be a number of radii (photon mean free paths) in length, the cylindrical conductivity Eq. 27 can be applied with a local radius y instead of b. The volume average of these local cylindrical conductivities gives the long needle Eq. 26.

The black body surface limit ($\epsilon \to 1$) is plotted on the back edge of the $\lambda_{r,\perp}(4\sigma\bar{T}^3 b)^{-1}$ surface of Figure 1a. The ϵ dependence of $\lambda_{r,\perp}$ is exclusively contained in $\chi_{0,\perp}$, $\chi_{1,\perp}$, and $\chi_{2,\perp}$, each with a factor $\epsilon(1-\epsilon)^{-1}$, and in the black body limit these terms in Eq. 13 become large to give

$$\lim_{\epsilon \to 1} \lambda_{r,\perp}(4\sigma\bar{T}^3 b)^{-1} = \lambda_{0,\perp} \qquad (28)$$

The α^2 dependence of $\lambda_{0,\perp}$ from Eqs. 17 and 19 can be seen in Figure 1b to increase in a slow monotone fashion from unity at $\alpha^2 = 0$ up to $3\pi/8(\approx 1.18)$ at $\alpha^2 = 1$.

The void radiation conductivity vanishes for a perfectly reflecting surface ($\epsilon \to 0$) as shown in the front edge of the Figure 1a surface. Another result of the explicit emissivity dependence of the $\chi_{i,\perp}$s mentioned in the previous paragraph is the ability to derive an analytical form of the slope at total reflection from Eqs. 13 and 14

$$d\left[\lambda_{r,\perp}(4\sigma\bar{T}^3 b)^{-1}\right]/d\epsilon|_{\epsilon=0} = (3/16)\left[(2+\alpha^{-2})(1-\alpha^2)^{1/2} + (4\alpha^2-1)\alpha^{-3}\arcsin\alpha\right]. \quad (29)$$

The slope decreases with increasing α^2 from unity at $\alpha^2 = 0$ for the spherical cavity down to $9\pi/32(\approx 0.88)$ for a long needle at $\alpha^2 = 1$. As a consequence, for a small emissivity value the long needle conductivity must be smaller than that of the corresponding sphere. While this decrease is rather small and difficult to see on the Figure 1a surface, the modest monotone decrease does appear in Figure 1b for $\epsilon = 0.1$. Equating the sphere (Eq. 25) and long needle (Eq. 26) conductivities provides the emissivity crossover value

$$\epsilon = (32 - 9\pi)/8 \approx 0.47 \quad (30)$$

below which, with increasing α^2 from zero to one, a net conductivity decrease occurs and above which a net conductivity increase occurs. However, Figure 1b also shows that overall changes in $\lambda_{r,\perp}$ with shape are not very significant unless $\epsilon > 0.6$.

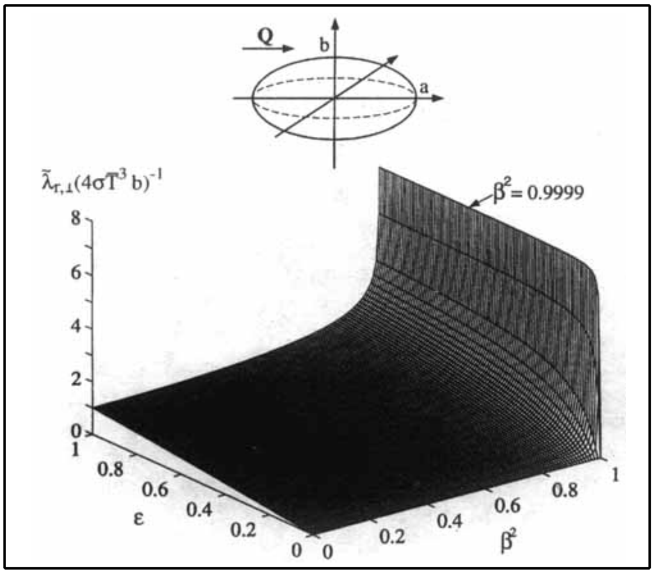

Figure 2a. Dimensionless radiation thermal conductivity $\tilde{\lambda}_{r,\perp}(4\sigma\bar{T}^3 b)^{-1}$, transverse to the symmetry axis of an oblate cavity, vs. the surface emissivity ϵ and squared eccentricity $\beta^2(= 1 - b^2a^{-2})$.

A sketch of the oblate ellipsoid along with the overall heat flux vector Q is included.

Oblate cavity, $\tilde{\lambda}_{r,\perp}$

A scheme was outlined in the beginning of the "Results" section to calculate void radiation conductivities that included oblate spheroids. In Figure 2a the dimensionless radiation conductivity $\tilde{\lambda}_{r,\perp}(4\sigma\bar{T}^3 b)^{-1}$ for transport transverse to the symmetry axis of an oblate cavity is shown for various values of the squared compression eccentricity $\beta^2[= 1 - b^2a^{-2}]$ from 0 to 1 and for the full range of surface emissivities ϵ from 0 to 1. An oblate cavity sketch is also shown with the direction of the overall heat flux Q. The surface of Figure 2a provides both a general picture of the effects of compression and surface emissivity on transverse oblate cavity radiation, as well as an opportunity to investigate the physical phenomena at the four limits $\beta^2 \to 0$, $\epsilon \to 1$, $\beta^2 \to 1$, and $\epsilon \to 0$. Figure 2b, which gives the $\tilde{\lambda}_{r,\perp}(4\sigma\bar{T}^3 b)^{-1}$ variation with emissivity ϵ for various β^2, is also included, and accurately displays the plateau, the knee, and the abrupt drop that characterizes the divergence of $\tilde{\lambda}_{r,\perp}$ in the neighborhood of $\beta^2 \to 1$.

The spherical cavity limit $\beta^2 \to 0$ is the same as the prolate case (Eq. 25)

$$\lim_{\beta^2 \to 0} \tilde{\lambda}_{r,\perp}(4\sigma\bar{T}^3 b)^{-1} = \epsilon \quad (31)$$

and the lefthand side of the Figure 2b surface exhibits the linear increase from zero to unity predicted by Eq. 31. Also similar to the prolate cavity, the $\tilde{\chi}_{i,\perp}$ divergence as $\epsilon(1-\epsilon)^{-1}$ in the black body limit $\epsilon \to 1$ from Eqs. 15, 16, and 18 generates from the oblate cavity version of Eq. 13

$$\lim_{\epsilon \to 1} \tilde{\lambda}_{r,\perp}(4\sigma\bar{T}^3 b)^{-1} = \tilde{\lambda}_{0,\perp} \quad (32)$$

The β^2 dependence of $\tilde{\lambda}_{0,\perp}$ from Eqs. 18 and 20 provides the backside variation of the dimensionless radiation conductivity in Figure 2a. $\tilde{\lambda}_{r,\perp}(4\sigma\bar{T}^3 b)^{-1}$ for a black body begins a slow increase from unity at $\beta^2 = 0$, but, suddenly, for squared eccentricities $\beta^2 > 0.8$ diverges to infinity.

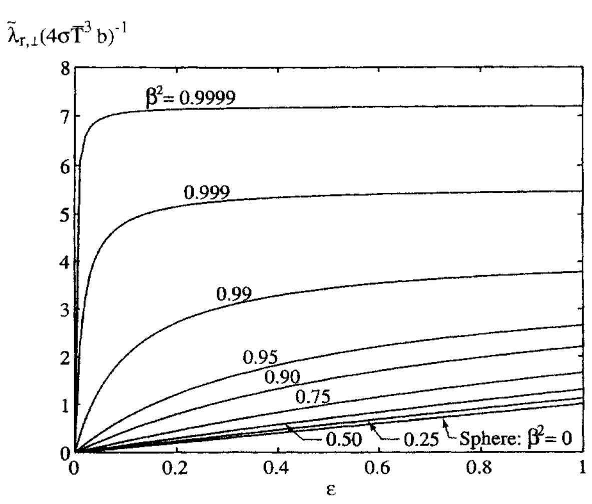

Figure 2b. Corresponding radiation conductivity vs. emissivity for various eccentricities.

The radiation conductivity transverse to the oblate cavity symmetry axis becomes infinite in limit of a thin discus $\beta^2 \rightarrow 1$, as shown in Figure 2b. As β^2 crosses 0.99 on its way to unity, plateaus are seen to develop in Figure 2b. They imply that $\tilde{\lambda}_{r,\perp}$ becomes independent of the emissivity over the plateau. The plateau thermal radiation conductivity values, $\tilde{\lambda}_{0,\perp}$ of Eq. 31, are given by the right-hand side black body intercept. These plateaus do not travel all the way across Figure 2b, but end abruptly at a knee, and then $\tilde{\lambda}_{r,\perp}$ drops rapidly to zero at $\epsilon = 0$. As β^2 approaches unity the knee appears to move over to the perfect reflector axis $\epsilon = 0$, and in the limit $\tilde{\lambda}_{r,\perp}$ becomes an infinitely high horizontal line in the manner

$$\left[\tilde{\lambda}_{r,\perp}(4\sigma\bar{T}^3 b)^{-1}\right]_{\beta^2 \rightarrow 1} \rightarrow -(3/4)\ln(1-\beta^2), \quad 0 < \epsilon \leq 1 \tag{33}$$

where Eq. 5 has been recast in dimensionless form appropriate for discussion of Figures 2a and 2b. In this limit $\beta^2 \rightarrow 1$ the trial temperature (Eq. 6) and radiosity are exact solutions to the problem. In the discus limit, the surfaces are flat, the surface normal component $\boldsymbol{\theta}_{\perp}/\theta_{\perp} \cdot \boldsymbol{\eta}$ transverse to the symmetry axis becomes very small, the radiosity form Eq. 7 for B^* approaches the black body radiosity, and both $\tilde{\lambda}_{e,\perp}$ and $\tilde{\lambda}_{r,\perp}$ become emissivity-independent, that is, the plateaus of Figure 2b. The edges become perfect insulators in the $\beta^2 \rightarrow 1$ limit because the plate spacing goes to zero at the extreme edges of the discus. In the kinetic theory of Knudsen diffusion through long slits, Berman (1965) obtained a singularity in the diffusivity as an *upper bound*. In the $\beta^2 \rightarrow 1$ limit, the discus can be regarded as slits in series with varying plate spacing. To the best of our knowledge an *exact* form (Eq. 33) of a long slit transport coefficient divergence is new.

The front part of the $\tilde{\lambda}_{r,\perp}(4\sigma\bar{T}^3 b)^{-1}$ surface of Figure 2a correctly vanishes as $\epsilon \rightarrow 0$. The emissivity slope, like the prolate cavity, can also be calculated for $\epsilon \rightarrow 0$ from Eqs. 13 and 15

$$\begin{aligned} d\left[\tilde{\lambda}_{r,\perp}(4\sigma\bar{T}^3 b)^{-1}\right]/d\epsilon|_{\epsilon=0} \\ = (3/32)\{2(3\beta^2-1)\beta^{-2}(1-\beta^2)^{-1} \\ + (3\beta^2+1)\beta^{-3}\ln[(1+\beta)/(1-\beta)]\} \end{aligned} \tag{34}$$

Near the limit $\beta^2 \rightarrow 1$, the slope (Eq. 34) exhibits the rapid change in the transverse conductivity value from Figures 2a and 2b, which can now be seen from the low emissivity side as a singular slope

$$\left\{d\left[\tilde{\lambda}_{r,\perp}(4\sigma\bar{T}^3 b)^{-1}\right]/d\epsilon|_{\epsilon=0}\right\}_{\beta^2 \rightarrow 1} \rightarrow (3/8)(1-\beta^2)^{-1} \tag{35}$$

Although near the limit $\beta^2 \rightarrow 1$ an emissivity independent $\tilde{\lambda}_{r,\perp}$ of Eq. 33 is a natural consequence of the oblate cavity shape, at the point $\epsilon = 0$ there can be no radiation emitted or absorbed by the cavity–solid interface and $\tilde{\lambda}_{r,\perp}$ must vanish.

Conclusions

For those complex engineering systems in which heat transfer is coupled to mass transport, chemical reactions, phase transitions, or internal structural changes, analytical forms for λ_e and λ_r will be much less computationally demanding to use. The physical problem considered is steady-state radiation heat transfer within prolate cavities with varying elongation and oblate voids of arbitrary compression. The process is inherently anisotropic with prolate cavity radiation conductivities parallel $\lambda_{r,\parallel}$ or transverse $\lambda_{r,\perp}$ to the symmetry axes with a corresponding set $\tilde{\lambda}_{r,\parallel}$ and $\lambda_{r,\perp}$ for the oblate cavity. The parallel conductivities were presented earlier, $\lambda_{r,\parallel}$ in Fitzgerald and Strieder (1997a) and $\tilde{\lambda}_{r,\parallel}$ in Fitzgerald and Strieder (1997b). As discussed later in the Appendix, the transverse conductivities presented in this article $\lambda_{r,\perp}$, $\tilde{\lambda}_{r,\perp}$ involve algebraically more complex integrals. It is interesting to note that the eccentricity–emissivity surfaces of both the pairs $\lambda_{r,\parallel}$, $\tilde{\lambda}_{r,\perp}$ and $\lambda_{r,\perp}$, $\tilde{\lambda}_{r,\parallel}$ have some similar features, but as the first pair member relates to a cylinder geometry and the second relates to a slit or parallel plates, quantitative differences are significant.

Equation 9 for $\boldsymbol{\lambda}_e$ provides a rigorous "best" estimate effective conductivity of a solid with prolate or oblate cavities of a single orientation and at lower void fractions. A rearrangement of Eq. 11 yields for the perpendicular case

$$\frac{\lambda_{e,\perp}(V.P.)}{\lambda_s} = \Lambda_{\perp} = 1 + \phi\frac{(\lambda_{r,\perp}-\lambda_s)}{(\lambda_{r,\perp}-\lambda_s)G_{\perp}(0)+\lambda_s} \tag{36}$$

whereas the parallel effective conductivity is

$$\frac{\lambda_{e,\parallel}(V.P.)}{\lambda_s} = \Lambda_{\parallel} = 1 + \phi\frac{(\lambda_{r,\parallel}-\lambda_s)}{(\lambda_{r,\parallel}-\lambda_s)(1-2G_{\perp}(0))+\lambda_s} \tag{37}$$

Values of $G_{\perp}(0)$ are given by the integral in Eq. 6c and $\lambda_{r,\perp}$ is obtained from Eqs. 13–24. The expression for $\lambda_{r,\parallel}$ has the same form as Eq. 13 for $\lambda_{r,\perp}$; however, the six prolate χ_i and λ_i functions ($i = 0, 1, 2$) for $\lambda_{r,\parallel}$, listed in Fitzgerald and Strieder (1997a) and the corresponding oblate functions in Fitzgerald and Strieder (1997b) are different. With mutually random spheroid orientation and at low void fraction, a simple angular average of Eq. 9

$$\lambda_e = \frac{1}{3}\lambda_{e,\parallel} + \frac{2}{3}\lambda_{e,\perp} \tag{38}$$

should provide sufficient accuracy for heat-transfer calculations. Note that in the limit of the spherical inclusion, $G_{\perp}(0) = 1/3$, Eqs. 36–38 reduce to the well-known Clausius-Mossotti equations (Landauer, 1977). Eqs. 36–38 for the effective conductivity are linear in the void fraction, and are referred to in the ceramic literature as the Loeb equation. While the Loeb equation has been used (Takahashi and Kikuchi, 1980) for higher voidages, its use for *a priori* predictions of λ_e is not recommended at void fractions above 10%.

For void fractions up to 30% with spheroidal inclusions, approximate equations are available (Landauer, 1977). Applications of the Lorentz average field theory to a two-Fourier model with anisotropic prolate or oblate ellipsoids placed at random, but aligned with symmetry axes parallel, has been treated by Bragg and Pippard (1953). Their results provide an extension of $\Lambda_\perp$ of Eq. 36 of the form

$$\frac{\lambda_{e,\perp}\,(\text{Lorentz})}{\lambda_s} = 1 + \phi \frac{(\lambda_{r,\perp} - \lambda_s)}{(1-\phi)(\lambda_{r,\perp} - \lambda_s)G_\perp(0) + \lambda_s} \tag{39}$$

and $\Lambda_\parallel$ of Eq. 37

$$\frac{\lambda_{e,\parallel}\,(\text{Lorentz})}{\lambda_s} = 1 + \phi \frac{(\lambda_{r,\parallel} - \lambda_s)}{(1-\phi)(\lambda_{r,\parallel} - \lambda_s)(1 - 2G_\perp(0)) + \lambda_s} \tag{40}$$

where Eq. 38 can again be used in practice to treat random orientation (Marino, 1971). Equations 39 and 40 differ from Eqs. 36 and 37 only in the factor $(1-\phi)$ in the denominator and become identical for small ϕ. Again, Eqs. 36–40 hold for the oblate cavities with tildes to indicate the a, b interchange.

Finally, we should give a word of caution. Marino's (1971) equation for the effective conductivity of a bed of spheroids oriented at random in three dimensions is not correct. Marino's conductivity, derived from Fricke (1924), is in error because the average field for a bed of spheroids with symmetry axes aligned parallel and for aligned spheroids perpendicular to the applied field were assumed to be equal. This cannot be true. In contrast, Eqs. 36–40 are based on the same modeling assumptions used by Fricke and Marino, but without the restrictive equality between the parallel and perpendicular average fields.

Notation

$G_\perp, \tilde{G}_\perp$ = general ellipsoidal temperature perturbation functions transverse to the symmetry axis for the prolate and oblate ellipsoids, defined by Eq. 6c

$\boldsymbol{i}$ = unit vector in the symmetry axis direction

$\lambda_{e,\perp}, \tilde{\lambda}_{e,\perp}$ = components of the effective conductivity transverse to the symmetry axis of a prolate and oblate cavity

$\lambda_{r,\perp}, \tilde{\lambda}_{r,\perp}$ = components of the radiation conductivity perpendicular to the symmetry axis of a prolate and oblate cavity

λ_s = solid conductivity

$\mu_\perp, \omega_\perp, \tilde{\mu}_\perp, \tilde{\omega}_\perp$ = prolate and oblate radiosity variational parameters transverse to the symmetry axis

$\boldsymbol{\theta}, \boldsymbol{\theta}_\perp$ = applied steady state temperature gradient and its component transverse to the symmetry axis

ϕ = void fraction

Literature Cited

Argo, W. B., and J. M. Smith, "Heat Transfer in Packed Beds," *Chem. Eng. Prog.*, **49**, 443 (1953).

Berman, A. S., "Free Molecule Transmission Probabilities," *J. Appl. Phys.*, **36**, 3356 (1965).

Bragg, W. L., and A. B. Pippard, "The Form Birefringence of Macromolecules," *Acta. Cryst.*, **6**, 865 (1953).

Carslaw, M. S., and J. C. Jaeger, *Conduction of Heat in Solids*, Oxford, London (1959).

Chiew, Y. C., and E. D. Glandt, "Simultaneous Conduction and Radiation in Porous Composite Material: Effective Thermal Conductivity," *Ind. Eng. Chem. Fundam.*, **22**, 276 (1983).

Fitzgerald, S. P., and W. Strieder, "Radiation Heat Transfer Down an Elongated Spheroidal Cavity," *AIChE J.*, **43**, 2 (1997).

Fitzgerald, S. P., and W. Strieder, "Radiation Heat Transfer Across a Compressed Spheroidal Cavity," *AIChE J.*, **43**, 2368 (1997).

Fitzgerald, S. P., "The Effect of Shape and Orientation upon Radiation Heat Transfer Within an Enclosed Cavity of a High Temperature Material," PhD Thesis, Univ. of Notre Dame (1998).

Fricke, H., "A Mathematical Treatment of the Electric Conductivity and Capacity of Disperse Systems," *Phys. Rev.*, **24**, 575 (1924).

Kaganer, M. G., *Thermal Insulation in Cryogenic Engineering*, IPST Press, Jerusalem (1969).

Landauer, R., "Electrical Conductivity in Inhomogeneous Media," *Electrical Transport and Optical Properties of Inhomogeneous Media*, No. **40**, J. C. Garland, and P. B. Tanner, eds., *Amer. Inst. of Phys.*, New York, p. 2 (1978).

Marino, G. P., "Radiation Transfer Across a Spherical Pore in a Linear Temperature Gradient," *Trans. Metall. Soc. of AIME*, **245**, 821 (1969).

Marino, G. P., "The Porosity Correction Factor for the Thermal Conductivity of Ceramic Fuels," *J. Nucl. Mat.*, **38**, 178 (1971).

McQuarrie, D. A., *Statistical Mechanics*, Harper Collins, New York (1973).

Ralston, A., and P. Rabinowitz, *A First Course in Numerical Analysis*, McGraw-Hill, New York (1978).

Siegel, R., and J. R. Howell, *Thermal Radiation Heat Transfer*, 3rd ed., McGraw-Hill, New York (1992).

Smith, J. M., *Chemical Engineering Kinetics*, 2nd ed. (1970), 3rd ed., McGraw-Hill, New York (1981).

Strieder, W., and S. Prager, "Upper and Lower Bounds on Knudsen Flow Rates," *J. Math. Phys.*, **3**, 514 (1967).

Takahashi, T., and T. Kikuchi, "Porosity Dependence of Thermal Diffusivity and Thermal Conductivity of Lithium Oxide Li_2O from 200 to 900°C," *J. Nucl. Mat.*, **91**, 93 (1980).

Tsai, D. S., and W. Strieder, "Radiation Across a Spherical Cavity Having both Specular and Diffuse Reflectance Components," *Chem. Eng. Sci.*, **41**, 170 (1985).

Tsai, D. S., and W. Strieder, "Specular and Diffuse Reflections in Radiant Heat Transport Across and Down a Cylindrical Pore," *Ind. Eng. Chem. Fundam.*, **25**, 244 (1986).

Varma, A., G. Cao, and M. Morbidelli, "Self-Propagating Solid-Solid Noncatalytic Reactions in Finite Pellets," *AIChE J.*, **36**, 1039 (1990).

Vortmeyer, D., "Radiation in Packed Solids," *Ger. Chem. Eng.*, **3**, 124 (1980).

Whitaker, S., "Radiant Energy Transport in Porous Media," *I. & E. C. Fundam.*, **19**, 210 (1980).

Appendix

The expressions (Eqs. 13–24) developed for $\lambda_{r,\perp}$ and $\tilde{\lambda}_{r,\perp}$ have been given in the article. The purposes of this appendix are to provide the formal definitions of the χ and λ functions of Eq. 13 that come from the rigorous variational calculation and give at least one intermediate form in the derivations of Eqs. 14–24 from the formal definitions.

The $\chi_{i,\perp}$ functions ($i = 0, 1, 2$) for a prolate cavity are integrals of the surface element $d^2\boldsymbol{r}$ over the cavity–solid interface Σ of the form,

$$b^{1-i}\chi_{i,\perp} = \epsilon(1-\epsilon)^{-1} 3(4\pi ab^2)^{-1} \int_\Sigma d^2\boldsymbol{r}[\boldsymbol{\zeta}\cdot\boldsymbol{r}]^{2-i}[\boldsymbol{\zeta}\cdot\boldsymbol{\eta}]^i, \qquad i = 0, 1, 2 \tag{A1}$$

where $\boldsymbol{\zeta}$ is a unit vector perpendicular to the prolate cavity symmetry axis, a is the semimajor axis, b is the semiminor axis, $\boldsymbol{r}$ is a vector from the cavity center, and $\boldsymbol{\eta}$ is a surface normal pointing into the cavity from point $\boldsymbol{r}$ on Σ. Using the geometrical integration quantities taken from Figure 1 of Fitzgerald and Strieder (1997a) we can recast the surface integral Eq. A1 into terms involving angular ψ' and symmetry axis x integrations

$$b^{1-i}\chi_{i,\perp} = \left(\frac{\epsilon}{1-\epsilon}\right)\left(\frac{3}{4\pi ab^2}\right)\int_{-a}^{a} dx \left(1-\frac{x^2\alpha^2}{a^2}\right)^{1/2}\left(1-\frac{x^2}{a^2}\right)^{-1/2}$$

$$\times\int_0^{2\pi} d\psi' b\left(1-\frac{x^2}{a^2}\right)^{1/2}\left[b\left(1-\frac{x^2}{a^2}\right)^{1/2}\cos\psi'\right]^{2-i}$$

$$\times\left[-\left(1-\frac{x^2}{a^2}\right)^{1/2}\left(1-\frac{x^2\alpha^2}{a^2}\right)^{-1/2}\cos\psi'\right]^{i} \quad \text{(A2)}$$

A comparison of the two square bracketed expressions in Eq. A2 with the corresponding terms in Eq. A4 of Fitzgerald and Strieder (1997a) (that is, $\boldsymbol{\zeta}\cdot\boldsymbol{r}$ and $\boldsymbol{\zeta}\cdot\boldsymbol{\eta}$ vs. $\boldsymbol{i}\cdot\boldsymbol{r}$ and $\boldsymbol{i}\cdot\boldsymbol{\eta}$) shows the x dependence of the terms in Eq. A2 above is substantially more complex. Nevertheless, the x integrations can be done exactly, and the integration of A2 for $i = 0, 1, 2$ gives Eqs. 14, 16 and 17.

As already discussed in the Introduction, b is a maximum circular cross-sectional radius for the prolate cavity, whereas for the oblate cavity b is the symmetry axis. The fact that the same ellipse is used to generate the prolate and oblate volumes of revolution, however, can be used to obtain the oblate version of Eq. A2. To do this, on the left-hand side of Eq. A2 change only the meaning of b, as pointed out above, and place a tilde over the $\chi_{i,\perp}$, but in the righthand side of Eq. A2 interchange all as and bs. In this process, note that $\alpha^2 = 1 - b^2a^{-2}$ in Eq. A2 *before* the a, b interchange, and that it is convenient to use $\beta^2 = 1 - b^2a^{-2}$ in Eq. A2 *after* the interchange.

The $\lambda_{i,\perp}$ functions ($i = 0, 1, 2$) for the prolate cavity require a double integral, with each surface element $d^2\boldsymbol{r}$ and $d^2\boldsymbol{r}'$ integrated independently over Σ.

$$b^{1-i}\lambda_{i,\perp} = 3(2\pi ab^2)^{-1}\int_\Sigma d^2\boldsymbol{r}\int_\Sigma d^2\boldsymbol{r}' K(\boldsymbol{r},\boldsymbol{r}')$$

$$\times[\boldsymbol{\zeta}\cdot(\boldsymbol{r}'-\boldsymbol{r})]^{2-i}[\boldsymbol{\zeta}\cdot(\boldsymbol{\eta}'-\boldsymbol{\eta})]^{i} \quad \text{(A3)}$$

where $K(\boldsymbol{r},\boldsymbol{r}')d^2\boldsymbol{r}'$ is the differential view factor for cosine law emission and $\boldsymbol{\eta}'$ is the surface normal evaluated at $\boldsymbol{r}'$ on Σ.

The double integrals of Eq. 3 can be written in terms of angles ψ and ψ', both over 0 to 2π, as well as over both the axial symmetry axes integrations w and x from $-a$ to a, in the same manner as was done in Eq. 2. The angular integrations can be performed exactly and after much algebra a 2-D integral form of $\lambda_{i,\perp}$ for $i = 0, 1, 2$ results.

$$b^{1-i}\lambda_{i,\perp} = 3(16b^2a)^{-1}\int_{-a}^{a} dx\int_{-a}^{a} dw\{[N_i(x)+N_i(w)]$$

$$\times[1-\alpha^6|x-w|(2a^2+x^2+4xw+w^2-10a^2\alpha^{-2}$$

$$-6xw\alpha^{-2}+8a^2\alpha^{-4})g^{-3}]+\alpha^2M_i(1-\alpha^2)^{-1}(a^2-x^2)^{-1/2}$$

$$\times(a^2-w^2)^{-1/2}[(x-w)^2+2\alpha^2(1-\alpha^2)^2|x-w|(a^2-x^2)$$

$$\times(a^2-w^2)g^{-3}-\alpha^2|x-w|(2a^2\alpha^{-2}-2a^2-2xw\alpha^{-2}$$

$$+x^2+w^2)g^{-1}]\}, \quad \text{(A4)}$$

where

$$g = [(x+w)^2\alpha^4 - 4xw\alpha^2 + 4a^2(1-\alpha^2)]^{1/2}.$$

The functions N_i and M_i are different for each of the coefficients, $i = 0, 1, 2$. The first $\lambda_{0,\perp}$ integral Eq. A4 with the definitions

$$N_0(x) = (b/a)^2(a^2-x^2) \quad \text{(A5a)}$$

and

$$M_0 = -2(b/a)^2(a^2-x^2)^{1/2}(a^2-w^2)^{1/2} \quad \text{(A5b)}$$

can be recast in a form similar to $\chi_{2,\perp}$, which can be done exactly to give Eq. 1a. For the second $\lambda_{1,\perp}$ and the third $\lambda_{2,\perp}$ integrals (Eq. A4)

$$N_1(x) = -(b/a)(a^2-x^2)(a^2-x^2\alpha^2)^{-1/2} \quad \text{(A6a)}$$

$$M_1 = (b/a)(a^2-x^2)^{1/2}(a^2-w^2)^{1/2}[(a^2-x^2\alpha^2)^{-1/2}$$

$$+(a^2-w^2\alpha^2)^{-1/2}] \quad \text{(A6b)}$$

$$N_2(x) = (a^2-x^2)(a^2-x^2\alpha^2)^{-1} \quad \text{(A7a)}$$

and

$$M_2 = -2(a^2-x^2)^{1/2}(a^2-w^2)^{1/2}(a^2-x^2\alpha^2)^{-1/2}$$

$$\times(a^2-w^2\alpha^2)^{-1/2} \quad \text{(A7b)}$$

The 2-D integrals $\lambda_{1,\perp}$ and $\lambda_{2,\perp}$ must be evaluated numerically and are fitted to Padé forms (Eqs. 21 and 22). Again, the algebraic complexity of the dot products $\boldsymbol{\zeta}\cdot(\boldsymbol{r}'-\boldsymbol{r})$ and $\boldsymbol{\zeta}\cdot(\boldsymbol{\eta}'-\boldsymbol{\eta})$ in Eq. A3 perpendicular to the symmetry axis [x and w coordinates in Eq. A4], as compared to the simpler parallel components $\boldsymbol{i}\cdot(\boldsymbol{r}'-\boldsymbol{r})$ and $\boldsymbol{i}\cdot(\boldsymbol{\eta}'-\boldsymbol{\eta})$ that occur in the corresponding Eqs. 42–44 in Fitzgerald and Strieder (1997a), increases the difficulty of the problem. As in the $b^{1-i}\chi_{i,\perp}$ discussion above, the $b^{1-i}\lambda_{i,\perp}$ Eqs. A4a–A7a can be readily converted to the corresponding oblate $b^{1-i}\tilde{\lambda}_{i,\perp}$ forms, on the lefthand side of Eq. A4a by changing the meaning of b, placing a tilde over $\lambda_{i,\perp}$, and completely interchanging a and b, including $\alpha^2 = 1 - b^2a^{-2}$, on the right-hand side of Eqs. A4a–A7b.

Manuscript received May 18, 1998, and revision received Sept. 4, 1998.